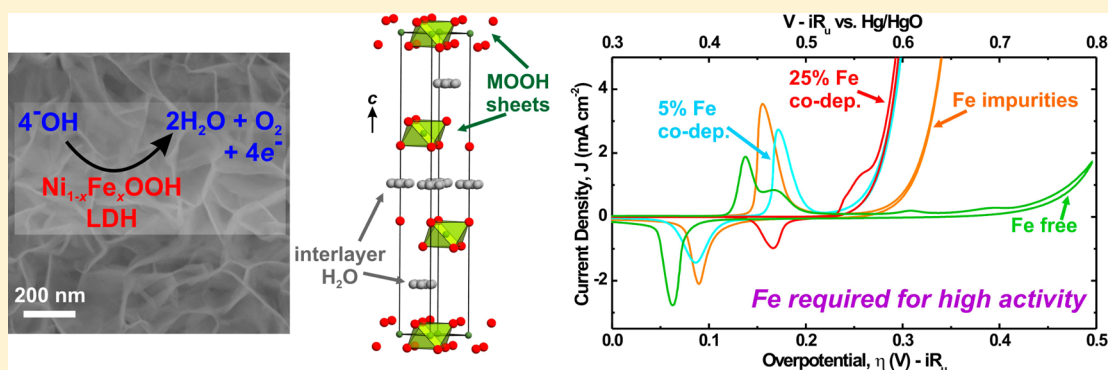# Nickel−Iron Oxyhydroxide Oxygen-Evolution Electrocatalysts: The Role of Intentional and Incidental Iron Incorporation

Lena Trotochaud, Samantha L. Young, James K. Ranney, and Shannon W. Boettcher*

Department of Chemistry and Biochemistry, University of Oregon, Eugene, Oregon 97403, United States

S *Supporting Information*

ABSTRACT: Fe plays a critical, but not yet understood, role in enhancing the activity of the Ni-based oxygen evolution reaction (OER) electrocatalysts. We report electrochemical, *in situ* electrical, photoelectron spectroscopy, and X-ray diffraction measurements on $Ni_{1−x}Fe_x(OH)_2$/$Ni_{1−x}Fe_xOOH$ thin films to investigate the changes in electronic properties, OER activity, and structure as a result of Fe inclusion. We developed a simple method for purification of KOH electrolyte that uses precipitated bulk $Ni(OH)_2$ to absorb Fe impurities. Cyclic voltammetry on rigorously Fe-free $Ni(OH)_2$/NiOOH reveals new Ni redox features and no significant OER current until >400 mV overpotential, different from previous reports which were likely affected by Fe impurities. We show through controlled crystallization that β-NiOOH is less active for OER than the disordered γ-NiOOH starting material and that previous reports of increased activity for β-NiOOH are due to incorporation of Fe-impurities during the crystallization process. Through-film *in situ* conductivity measurements show a >30-fold increase in film conductivity with Fe addition, but this change in conductivity is not sufficient to explain the observed changes in activity. Measurements of activity as a function of film thickness on Au and glassy carbon substrates are consistent with the hypothesis that Fe exerts a partial-charge-transfer activation effect on Ni, similar to that observed for noble-metal electrode surfaces. These results have significant implications for the design and study of $Ni_{1−x}Fe_xOOH$ OER electrocatalysts, which are the fastest measured OER catalysts under basic conditions.

1.0. INTRODUCTION

The electrolysis of water to form H_2 and O_2 gas (i.e., water splitting, $H_2O → H_2 + 1/2O_2$) could enable the large-scale storage of intermittent energy from the sun, wind, or other renewable sources.[1,2] The kinetically slow oxygen evolution reaction (OER) $2H_2O → 4H^+ + O_2 + 4e^−$ (in acid) or $4OH^− → 2H_2O + O_2 + 4e^−$ (in base) represents a significant efficiency loss in water-splitting systems.[2,3] Identifying more-efficient, stable, earth-abundant catalysts for the OER is a significant challenge.

$Ni_{1−x}Fe_xOOH$ oxyhydroxide electrocatalysts have been under intense study because they are the most active catalysts measured in basic media.[4−14] We previously compared thin films of OER catalysts deposited on quartz-crystal microbalance (QCM) electrodes and found that $Ni_{0.9}Fe_{0.1}OOH$ has an OER turnover frequency (TOF) >10-fold higher than that of IrO_x.[11] The high activity, along with the ability to deposit thin films with low optical absorption using solution-processing, makes $Ni_{1−x}Fe_xOOH$ catalysts appealing for use in solar water-splitting devices.[11,15−17] We note, however, that $Ni_{1−x}Fe_xOOH$ OER catalysts have been known for over 25 years,[14,18,19] and the measured activities (per-Ni) appear to vary little despite differences in synthesis.[4,8,10,20,21] Large-scale combinatorial screening has further shown that OER catalysts with both Ni and Fe have the highest activity.[20,22,23] The addition of other elements (e.g., Ce, Al, Co) may have additional effects, but does not appear to dramatically enhance the activity. Differences in intrinsic activity, however, are difficult to evaluate without a quantitative determination of a TOF.

Despite the large number of studies that indicate that both Ni and Fe are essential for high OER activity in a base, little progress has been made on understanding the role of Fe in increasing the OER activity. Corrigan proposed several

hypotheses, including that Fe enhances the electrical conductivity of NiOOH.[18] Electrochemical studies show an anodic shift of the Ni redox waves with increasing x in $Ni_{1-x}Fe_xOOH$,[8,9,18] indicating changes in the electronic structure. The details of these changes and their precise effect on the catalysis mechanism remain unknown.

Incorporation of Fe also changes the physical structure of $Ni(OH)_2/NiOOH$, but clear structure/activity relationships in $Ni_{1-x}Fe_xOOH$ OER catalysts have not been established. $Ni(OH)_2/NiOOH$ adopts a brucite (theophrasite) structure, with layers of metal-(oxy)hydroxide sheets separated by water and aqueous ions.[24,25] The redox activity and porous, hydrated, ion-permeable nature of $Ni(OH)_2/NiOOH$ indeed enable its use in commercial Ni-metal-hydride rechargeable batteries.[26] The registry and spacing between the layers are affected by the synthetic conditions, aging in basic electrolyte, and prolonged application of an oxidizing potential.[27−32] Earlier work using X-ray absorption[5,7,33] and Mössbauer[34−36] spectroscopies shows that Fe^{3+} substitutes for Ni^{2+} in α-$Ni(OH)_2$. Louie and Bell recently used *in situ* Raman spectroscopy to provide evidence that Fe in NiOOH modifies the Ni−O local environment, which correlates with increasing OER activity.[8]

One major challenge in understanding the fundamental role of Fe on NiOOH OER activity, electronic properties, and physical structure has been the difficulty in measuring rigorously Fe-free catalysts; sub-ppm levels of Fe in electrolyte readily incorporate in NiOOH.[11,18,37] Here we report a simple method using high-purity $Ni(OH)_2$ precipitate as an Fe-absorbent to remove trace Fe from KOH electrolyte. We then investigate the relationship between electrical conductivity, substrate type, and structural order on measured OER activities as a function of Fe content in $Ni_{1-x}Fe_xOOH$ films. Our major findings are that (1) Fe incorporation increases NiOOH conductivity >30-fold but that the increased conductivity is not sufficient to explain the increased activity in thin film samples; (2) contrary to previous findings in unpurified electrolytes (for example, see refs 8, 9, 32, and 38−42), pure NiOOH is a poor catalyst for OER independent of degree of order, and prolonged anodic polarization and/or aging in KOH electrolyte does not increase pure NiOOH activity; and (3) Fe affects the NiOOH electronic structure by inducing partial-charge transfer in a manner similar to the case of high-work-function surfaces studied by Bell and co-workers.[39,43] These results are critical to further elucidate periodic trends of pure metal (oxy)hydroxide OER activities,[44] compare experimental results with theoretical predictions,[45−48] and ultimately design catalysts with higher activity.

2.0. EXPERIMENTAL SECTION

2.1. Characterization. Microgravimetry measurements were made using a 5 MHz quartz crystal microbalance (Stanford Research Systems QCM200). The film mass was calculated from changes in resonance frequency using the Sauerbrey equation[49] $\Delta f = -C_f \times \Delta m$, where Δf is the observed frequency change (Hz), C_f is the sensitivity factor of the 5 MHz AT-cut quartz crystal (58.3 ± 3.7 Hz μg^{-1} cm^2; see ref 11 for description of C_f calibration), and Δm is the change in mass per unit area (μg cm^{-2}). Grazing incidence X-ray diffraction (GIXRD) patterns were recorded on a Philips X'Pert Panalytical diffractometer operating at 30 mA and 50 kV using monochromated Cu Kα_1 radiation (incident angle = 0.2°, λ = 1.541 Å, step size = 0.05°, integration time 25 s/step). Scanning electron microscopy (SEM) images were collected on a Zeiss Ultra 55 SEM at 5 kV. X-ray photoelectron spectroscopy (XPS) studies were carried out on an ESCALAB 250 (ThermoScientific) using a Mg Kα nonmonochro-

mated flood source (200 W, 75 eV pass energy). The use of a Mg source is critical for detecting low concentrations of Fe. Use of a typical Al source results in the overlapping of Ni LMM Auger features with the Fe 2p peaks, making detection of low Fe concentrations impossible. The samples were charge-neutralized using an in-lens electron source combined with a low-energy Ar$^+$ flood source. Spectra were analyzed, including satellite subtraction for the nonmonochromated X-ray source, using ThermoScientific Avantage 4.75 software. The C 1s peak for adventitious hydrocarbons at 285.0 eV was used for binding energy calibration.

2.2. Electrochemical Measurements. All electrochemical measurements were made in PTFE or polypropylene beakers containing a 1 M KOH electrolyte solution (Fluka Analytical TraceSelect, $\geq$ 30%, diluted with 18.2 MΩ·cm H$_2$O). Based on the lot analysis and assuming no Fe in the 18.2 MΩ·cm H$_2$O, we calculate <36 ppb Fe in the 1 M KOH solution. All electrochemical cell components were cleaned prior to experiments with 1 M H$_2$SO$_4$ and rinsed with copious quantities of 18.2 MΩ·cm H$_2$O. A BioLogic SP300 potentiostat was used operating in two-electrode mode for film deposition, three-electrode mode for cyclic voltammetry (CV) measurements, and four-electrode bipotentiostat mode (two synchronized working electrodes) for through-film conductivity measurements. A carbon cloth (Fuel Cell Earth, untreated) counter electrode was used for film deposition, while a Pt wire counter electrode housed in a custom polypropylene compartment separated by porous polypropylene was used for CV and conductivity measurements. Pt counter electrodes were cleaned periodically by dipping in aqua regia for ~20 s. A new piece of carbon cloth was used for each deposition solution. Potentials in three- and four-electrode modes were measured versus a 1 M KOH Hg/HgO reference electrode (CH Instruments). The potential of the 1 M KOH Hg/HgO reference was measured to be 0.928 V vs the reversible hydrogen electrode (RHE) in 1 M KOH. The RHE was fabricated by bubbling high-purity hydrogen over a freshly cleaned Pt coil in 1 M KOH. Samples deposited on QCM electrodes were connected to the working electrode lead of the potentiostat through the crystal face bias connector of the QCM200. Through-film conductivity measurements were made on Au/Ti/quartz interdigitated array (IDA) electrodes (ALS Co.; 2 μm line width, 2 μm gap, 2 mm length, 65 pairs). The reference and counter electrode leads on the IDA electrodes were not used. The voltammetry data presented here were collected on QCM Au/Ti electrodes unless otherwise indicated. For certain measurements, a glassy carbon (GC) rotating disk electrode (RDE) (Pine Instruments) was used at 1500 rpm.

High-purity O$_2$ gas was bubbled through the KOH electrolyte for at least 20 min prior to electrochemical measurements. Magnetic stirring was used to dislodge O$_2$ bubbles formed on the QCM electrode surface. Electrochemical data were corrected for uncompensated series resistance R_u, which was determined by equating R_u to the minimum total impedance in the frequency regime between 10 to 50 kHz where the capacitive and inductive impedances are negligible and the phase angle was near zero. R_u was ~1−3 Ω for QCM substrates and ~4−6 Ω for the GC-RDE substrate. The overpotential η was calculated using the equation $\eta = E_{measured} - E_{rev} - iR_u$, where $E_{measured}$ is the potential recorded vs Hg/HgO, E_{rev} is the reversible potential of the OER vs Hg/HgO (0.30 V in 1 M KOH calibrated as described above), and i is the current. Current densities are calculated using geometric surface areas.

2.3. Film Thickness and TOF Calculations. Effective film thicknesses were calculated by integrating the Ni$^{3+/2+}$ reduction wave, assuming 1 e$^-$ per Ni atom and a (001)-oriented $Ni(OH)_2$ film (i.e., a sheet of $Ni(OH)_2$ lying flat on the substrate surface) with an average monolayer thickness of 8 Å for α-$Ni(OH)_2$.[50] We label this an "effective" film thickness because the $Ni(OH)_2$ sheets do not all lie flat on the substrate. For films on QCM substrates, the assumption of 1 e$^-$ per Ni correlates well with the measured mass of deposited catalyst films and is consistent with our previous work.[11] We note that others have calculated up to ~1.67 e$^-$ per Ni,[29,30] meaning that the 1 e$^-$ per Ni used here may underestimate the intrinsic catalyst TOF.[41,51] For thicker films deposited for conductivity measurements, thicknesses were measured using a stylus profilometer.

Turnover frequency (TOF) values reported here are defined as the moles of O_2 evolved per mole of Ni in the catalyst per second. The TOFs are calculated at specified series-resistance-corrected overpotentials by averaging the current of the forward and reverse CV sweeps (taken at a scan rate of 10 mV s^{-1}), subtracting the average current of the forward and reverse sweeps of the bare substrate at the same overpotential, and dividing by the moles of Ni determined as described above.

2.4. KOH Electrolyte Purification. For rigorously Fe-free measurements, the 1 M KOH electrolyte was purified as follows. In a H_2SO_4-cleaned 50 mL polypropylene centrifuge tube, ~2 g of 99.999% $Ni(NO_3)_2 \cdot 6H_2O$ were dissolved in ~4 mL of 18.2 MΩ·cm H_2O. 20 mL of 1 M KOH were added to precipitate high-purity $Ni(OH)_2$. The mixture was shaken and centrifuged, and the supernatant was decanted. The $Ni(OH)_2$ then underwent three washing cycles by adding ~20 mL of 18.2 MΩ·cm water and ~2 mL of 1 M KOH to the tube, redispersing the solid, centrifuging, and decanting the supernatant. Finally, the tube was filled with 50 mL of 1 M KOH for purification. The solid was redispersed and mechanically agitated for at least 10 min, followed by at least 3 h of resting. The mixture was centrifuged, and the purified KOH supernatant was decanted into a H_2SO_4-cleaned polypropylene bottle for storage.

2.5. Film Deposition. Prior to film deposition, substrates were cycled three times in 1 M KOH from 0.0−0.8 V vs Hg/HgO. Substrates were rinsed with 18.2 MΩ·cm H_2O before being transferred to the deposition solution. Films of $Ni(OH)_2$ were cathodically deposited from unstirred solutions of 0.1 M $Ni(NO_3)_2 \cdot 6H_2O$ (Sigma-Aldrich, 99.999% trace metals basis) in 18.2 MΩ·cm H_2O. As-deposited $Ni(OH)_2$ films showed no XPS signal for Fe (see discussion below). For films containing codeposited Fe, the total metal content in the deposition solution was held at 0.1 M, and $FeCl_2 \cdot 4H_2O$ (Sigma-Aldrich, >98%) was added. The solutions were purged with N_2 gas for at least 20 min before adding $FeCl_2 \cdot 4H_2O$ to prevent precipitation of insoluble FeOOH. Typical depositions at −0.1 mA cm^{-2} for 120 s gave effective film thicknesses of ~40 nm (see Figure S1 in the Supporting Information for a typical deposition profile and QCM frequency measurement). After deposition, films were rinsed by dipping in H_2O before being transferred to the electrochemical cell. The Fe/Ni ratio in the films was higher than that in the deposition solutions; however, any given Fe content in solution consistently produced films with the same Fe content (< ± 4%) as determined by XPS. All film Fe contents reported here are those measured by XPS.

3.0. RESULTS AND DISCUSSION

3.1. Fe Impurities and Their Removal. The ability to make rigorously Fe-free control measurements on $Ni(OH)_2$/NiOOH is critical for understanding the role of Fe. Previous work has shown that Fe impurities readily incorporate into $Ni(OH)_2$/NiOOH films during electrochemical experiments.[11,18] Corrigan showed that Fe-impurity levels as low as 1 ppm in KOH electrolyte significantly affect the activity of $Ni(OH)_2$, particularly for thinner films where the incorporated Fe makes up a larger percentage of the film.[18] To minimize the effects of Fe impurities, we eliminated all glass components from our electrochemical cell (which are etched by KOH), cleaned all cell components with H_2SO_4 before each experiment, used the highest purity KOH electrolyte available, and used high-purity $Ni(NO_3)_2$ (99.999%) for film deposition. As shown in Figure 1a, no Fe is detected by XPS in as-deposited $Ni(OH)_2$ films. Despite these precautions, we find significant Fe incorporation into $Ni(OH)_2$ after electrochemical experiments.

Figure 1b shows a series of CV cycles of a $Ni(OH)_2$ film deposited on a GC-RDE. At a rotation rate of 1500 rpm, OER activity increases with each CV cycle. The Fe 2p XPS signal (Figure 1a) is evident after 5 CV cycles, and the atomic ratio of Ni/Fe is quantified as 95:5. XPS depth profiling shows that,
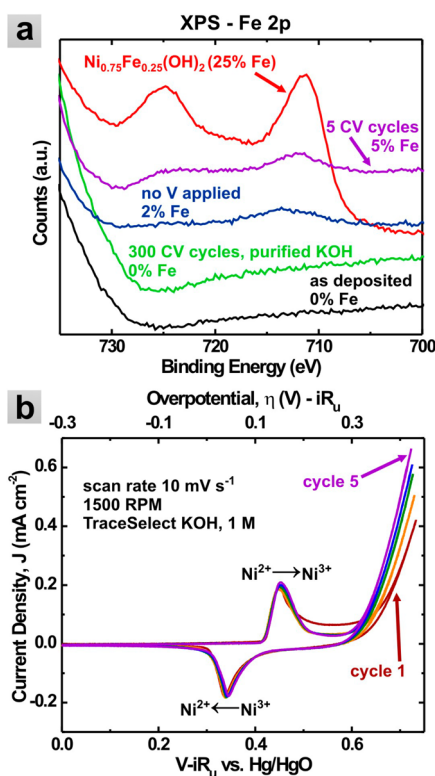

Figure 1. (a) XPS Fe 2p spectra for $Ni(OH)_2$/NiOOH thin films after 5 CV cycles in TraceSelect KOH (purple), 12 min in TraceSelect KOH electrolyte with no applied potential (blue), and 300 CV cycles in purified KOH (green). Spectra for an as-deposited film containing no Fe (black) and a film with 25% codeposited Fe (red) are shown for reference. The increase in intensity for binding energies above ~730 eV is due to the onset of an O KLL Auger peak. Spectra are offset on the y-axis for clarity. (b) Cyclic voltammogram of a $Ni(OH)_2$ film deposited on a GC-RDE. With each subsequent CV cycle, OER current increases due to Fe incorporation.

after only 5 CV cycles, Fe is incorporated throughout the film and not just at the film surface (see Figure S2), consistent with the electrolyte-permeable structure and previous results from Auger electron spectroscopy depth profiling.[18] The film spent a total of ~12 min rotating in the electrochemical cell from beginning to end of this CV experiment. Figure 1a shows that a different $Ni(OH)_2$ film which was simply rotated in the KOH electrolyte for 12 min (i.e., with no applied potential) also has significant Fe incorporation (98:2 Ni/Fe). In fact, the presence of Fe impurities in the KOH electrolyte also increases the OER activity of the bare Au substrate (see Figure S3), although an extensive analysis of these changes was not completed.

To measure the electrochemical behavior of Fe-free Ni-$(OH)_2$, we developed a simple purification procedure. As described above, we found that $Ni(OH)_2$ readily absorbs Fe without an applied potential. We therefore suspended high-purity $Ni(OH)_2$ powder prepared by precipitation (i.e., of the same composition as the catalyst) in the electrolyte to absorb all Fe impurities prior to electrochemical testing of Fe-free $Ni(OH)_2$ films. Figure 1a shows no detectable Fe 2p XPS signal in a $Ni(OH)_2$ film after 300 CV cycles in the purified electrolyte. All subsequent measurements were conducted in electrolyte purified by this method unless otherwise indicated.

3.2. Effects of Fe on Electrochemical Redox Behavior and Crystal Structure. Prolonged cycling or aging (in the absence of an applied potential) of $Ni(OH)_2$ electrodes in basic
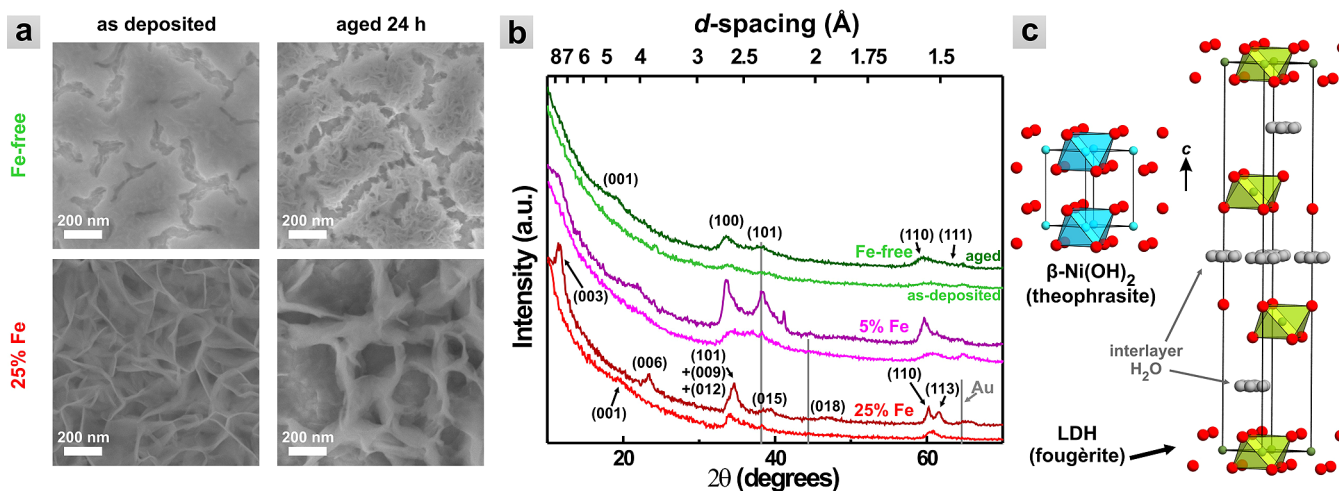
Figure 2. (a) SEM images of $Ni(OH)_2$ and $Ni_{0.75}Fe_{0.25}(OH)_2$ films as-deposited and after 24 h of aging in 40 °C 1 M KOH. (b) Grazing-incidence GIXRD patterns of $Ni_{1-x}Fe_x(OH)_2$ films for x = 0, 0.05, and 0.25 as-deposited (lower, lighter color shades) and after aging in 40 °C 1 M KOH for 24 h (upper, darker color shades). The pattern for the Au substrate is shown (in gray) for reference, and Au may contribute slightly to the intensity of the peaks near 38° 2θ and the background near 44.4° and 64.6° 2θ. The sloping background is due to the grazing-incidence geometry and has not been subtracted to preserve the peaks near 11° 2θ. Indices with the green pattern (top) are for β-$Ni(OH)_2$, and those with the red pattern (bottom) are for the Ni−Fe layered double hydroxide. (c) Crystal structures of β-$Ni(OH)_2$ (theophrasite; ICSD 28101) and NiFe-LDH (fougèrite; ICSD 159700; note that this is the all-Fe analogue) viewed roughly along the [110] direction. The unit cell edges are indicated by dark lines. Red = OH; blue = Ni^{2+}; green = Ni^{2+}/Fe^{3+}; gray = water. H atoms in both structures and interlayer anions in the LDH structure are omitted for clarity.

electrolyte has been shown to convert the disordered, as-deposited α-$Ni(OH)_2$ to the more crystalline β-form.[31,39,50,52−55] Multiple studies have concluded that β-$Ni(OH)_2$ is significantly more active for OER than the α-$Ni(OH)_2$.[40,50,56] Such observations are important in the context of understanding the role of three-dimensional structure on the OER activity, as well as in providing insight to guide theory.[48,57] Given the extreme sensitivity of the OER activity on Fe impurities,[18] it is possible that previous studies of β-$Ni(OH)_2$ formed by aging/recrystallization are contaminated with Fe. Furthermore, the role of crystallinity in $Ni_{1-x}Fe_xOOH$ with intentional Fe addition has not been previously studied and could provide additional insight into the enhanced activity.

The transition from as-deposited α-$Ni(OH)_2$ to β-$Ni(OH)_2$ can be observed by X-ray diffraction (see Figure S4 and also ref 50). For GIXRD experiments, films ~150−200 nm thick were deposited (10 min, −0.1 mA cm^{-2} cathodic) on Au substrates. Figure 2a shows SEM images of these films before and after aging in purified 1 M KOH at 40 °C for ~24 h. Films electrodeposited on Au have a spongy platelet-like structure. After aging, the average platelet size observed by SEM increases (from ~9 ± 2 nm to ~12 ± 3 nm in the Fe-free and ~20 ± 5 nm to ~35 ± 11 nm in the 25% Fe films shown here). In general, films containing Fe had a larger platelet size than those without Fe. Thinner films and films deposited on GC tended to be composed of smaller platelets (see Figures S5−S8 for additional SEM images of samples discussed in this work).

Figure 2b shows GIXRD patterns for films before and after aging. All diffraction patterns show increased peak intensity after aging, indicating an increase in the film crystallinity. The patterns obtained after aging for the Fe-free $Ni(OH)_2$ film agree with the pattern for β-$Ni(OH)_2$ (Figure S4 and ref 50). The peak near 19° 2θ corresponds to the (001) β-$Ni(OH)_2$ reflection whose intensity is related to the registry between the $Ni(OH)_2$ sheets along the c-axis (Figure 2c). The fact that the β-$Ni(OH)_2$ reflections remain relatively low intensity and broad could indicate the persistence of some disordered α-$Ni(OH)_2$,

which is consistent with voltammetry results that show two main oxidation waves after aging (see below).

The pattern of the as-deposited $Ni_{0.75}Fe_{0.25}(OH)_2$ also shows weak reflections associated with β-$Ni(OH)_2$. After aging $Ni_{0.75}Fe_{0.25}(OH)_2$, sharp peaks at ~11° and 23.5° 2θ emerge and the weak (001) β-$Ni(OH)_2$ reflection is further diminished. These new peaks match those of mixed Ni−Fe layered double hydroxides (NiFe-LDH; fougèrite/pyroaurite mineral structure) with 25−50% Fe synthesized by coprecipitation,[58] topochemical,[59] or mechanochemical[60] methods, with the peaks at ~11° 2θ and 23.5° 2θ corresponding to the (003) and (006) reflections, respectively. The NiFe-LDH unit cell is extended along the c-axis (~2 nm, depending on the identity of the interlayer anions) compared to that for β-$Ni(OH)_2$ (0.46 nm) and comprises three sheets of metal cations (see Figure 2c). The NiFe-LDH structure has a significantly larger intersheet spacing compared to that of β-$Ni(OH)_2$ because the increased charge of Fe^{3+} relative to Ni^{2+} is compensated by additional anions (and associated water) in-between the sheets.[34,35,61] (Note that the formal composition for hydrated NiFe-LDH structures is $[Ni^{II}_{1-x}Fe^{III}_x(OH)_2]^{x+}[x/nA^{n-}]^{x-} \cdot zH_2O$, where A = anions. We use the simpler $Ni_{1-x}Fe_x(OH)_2$ formula and have excluded the interlayer anions from Figure 2c for clarity.) The pattern for aged $Ni_{0.95}Fe_{0.05}(OH)_2$ shows both a peak at 11° 2θ, indicating a NiFe-LDH phase, and a weak broad peak at ~22° 2θ that is not directly assignable to either the NiFe-LDH or the pure β-$Ni(OH)_2$ phases. This peak at ~22° 2θ could be assignable to α-$Ni(OH)_2$ (see Figure S4), which also has water and ions between the metal-hydroxide sheets, although with a smaller intersheet spacing than the NiFe-LDH. It is therefore possible that $Ni_{0.95}Fe_{0.05}(OH)_2$ contains a mixture of NiFe-LDH and α-$Ni(OH)_2$ phases. All the diffraction data collected, however, are consistent with (1) increased crystallinity and long-range order perpendicular to the (00l) family of planes with aging (i.e., increased registry between the sheets) and (2) increased spacing between metal cation sheets in the catalyst films upon substitution of Fe^{3+} for
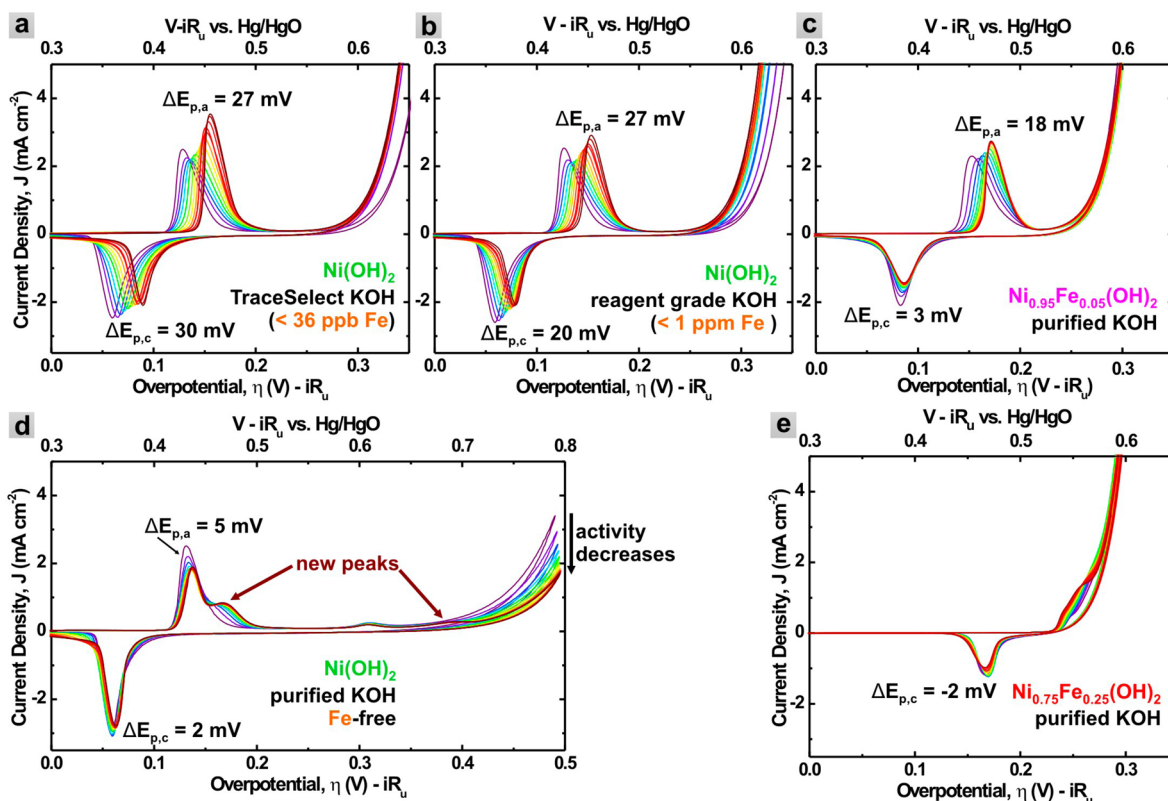
Figure 3. Cyclic voltammograms taken during aging of films in various purities of KOH. A total of 13 CV scans are shown for each sample; one for the initial as-deposited film (dark purple), and one additional scan after each 5 min aging period up to a total of 1 h of aging (dark red). The changes in the anodic and cathodic wave positions ($\Delta E_{p,a}$ and $\Delta E_{p,c}$) are labeled for each set of CVs. (No $\Delta E_{p,a}$ value is shown for the $Ni_{0.75}Fe_{0.25}(OH)_2$, as the oxidation wave is partially obscured by the OER current.)

Ni^{2+}. The increased intersheet spacing would be expected to facilitate OH^-/O_2 transport through the film, but would limit electronic interactions between active sites on adjacent layers along the c-axis.

Previous studies of the α-$Ni(OH)_2$ to β-$Ni(OH)_2$ transformation with aging report a corresponding anodic shift in the β-$Ni(OH)_2/\beta$-$NiOOH$ redox wave relative to that of the as-synthesized α-$Ni(OH)_2/\gamma$-$NiOOH$, as well as a lower onset potential for the OER on β-$NiOOH$ (e.g., see refs 8, 18, 27, 32, 50, and 62). These observations have long been interpreted to indicate that β-$Ni(OH)_2/\beta$-$NiOOH$ has an intrinsically higher OER activity than α-$Ni(OH)_2/\gamma$-$NiOOH$ due to its structure.[40,50] For example, Louie and Bell age $Ni(OH)_2$ films in 10 M KOH and observe a 40 mV anodic shift of the redox peaks and a 20-fold increase in OER activity at η = 0.3 V.[8] They argue that the incorporation of Fe impurities should be negligible due to the absence of an applied potential during the aging process, but the possibility of Fe incorporation cannot be conclusively ruled out as the lower detection limit of Fe for the elemental analysis used was reported to be ~3%. The anodic shift of redox waves and increases in OER activity are also indicative of Fe incorporation.[18] Our results show that, even in the absence of an applied potential (i.e., during aging in KOH electrolyte), Fe incorporation into $Ni(OH)_2$ does occur and significantly affects electrochemical behavior. The films investigated by Louie and Bell were approximately the same thickness (~70 nm) as those studied here (~40−60 nm), and thus we would expect the extent of Fe impurity incorporation to be similar (~2% of the total metal) or higher (due to the use of 10 M KOH aging solution).

To further study these effects we conducted systematic aging experiments for $Ni(OH)_2$, $Ni_{0.95}Fe_{0.05}(OH)_2$, and $Ni_{0.75}Fe_{0.25}(OH)_2$ films in different purity electrolytes. Films were subjected to 5 min periods of aging at 40 °C in 1 M KOH. After each aging period, CV data were collected. This process was repeated to give a total of 13 CV data sets (including as-deposited) and a total aging time of 60 min for each sample.

Figure 3a and b show the changes in CV behavior of $Ni(OH)_2$ in the presence of Fe impurities. When aged in either the TraceSelect KOH (Figure 3a) or reagent-grade KOH (Figure 3b) that was not subsequently purified, the redox peaks shift to higher potentials and the OER activity increases. In both electrolytes, the redox peaks shift by similar amounts. XPS shows Ni/Fe ratios of 96:4 and 92:8 after 1 h of aging in the TraceSelect-aged and reagent-grade-aged films, respectively. The OER activity increase is greater in the reagent-grade-aged films relative to those aged in the TraceSelect KOH, consistent with more Fe in reagent-grade KOH resulting in more Fe incorporation into the film. Films with coprecipitated Fe show little change in electrochemical behavior with aging even in the purified electrolyte. Films with 5% (Figure 3c) or 25% (Figure 3e) coprecipitated Fe show no change in OER activity. Only the oxidation wave for the sample with 5% Fe shifts to higher potentials. The lack of significant changes to the OER activity for $Ni_{0.75}Fe_{0.25}(OH)_2$ films as a function of aging (and hence crystallization) suggests that the long-range order and intersheet registry are unimportant for the active site OER activity. It also suggests that the OER activity is not related to structural defects within $Ni_{0.75}Fe_{0.25}OOH$, but inherent to the mixed Ni−Fe oxyhydroxide sheet.
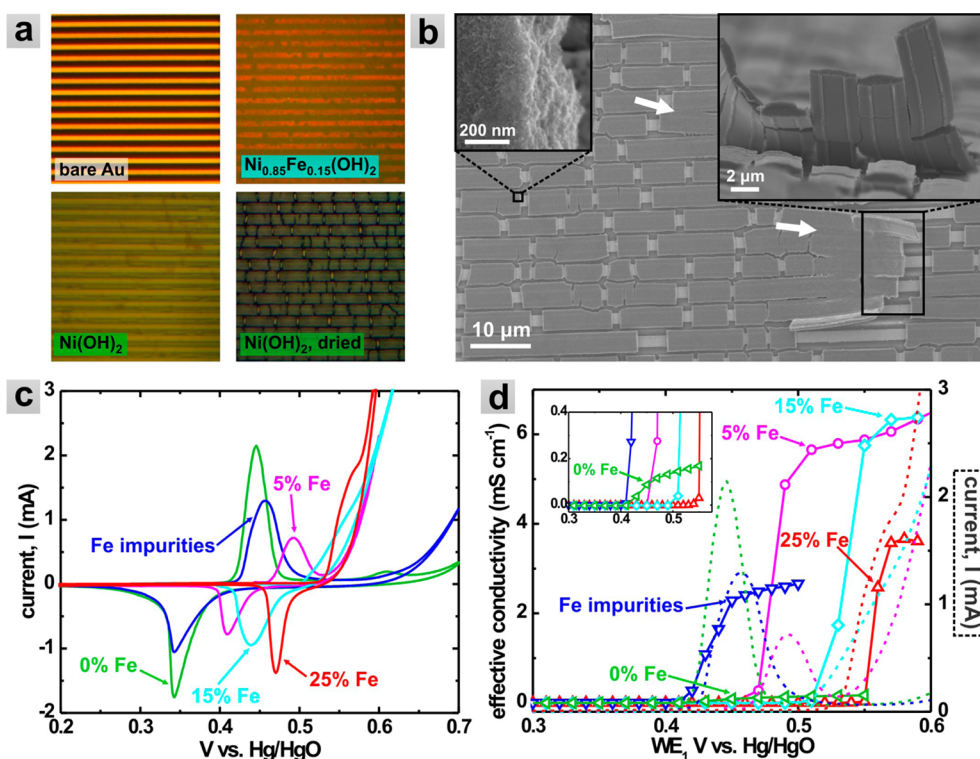
Figure 4. (a) Optical microscope images of IDA electrodes bare and with deposited films. Upon drying, cracking of the films is observed, but the films are crack free when kept wetted. (b) SEM images of $Ni(OH)_2$ film on an IDA electrode. Despite cracking, continuous regions of the film can be seen which span the gap spaces (indicated by white arrows). (c) CV scans of $Ni_{1-x}Fe_x(OH)_2/Ni_{1-x}Fe_xOOH$ films deposited on IDA electrodes. Currents are not normalized for differences in film thickness, and potential values are not corrected for series resistance. (d) Conductivity data (points with solid connecting lines) for the same films. The potential onset of conductivity correlates with the position of the hydroxide/oxyhydroxide oxidation wave shown as dotted lines for each film. The inset shows an enlarged region to make the conductivity turn-on for the rigorously Fe-free film apparent.

The electrochemical behavior of $Ni(OH)_2$ films aged in purified KOH electrolyte is different from that of previous reports[8−10,19,36,38−41,50,62−66] and different from what we observe in the unpurified electrolyte. First, instead of a gradual anodic shift in the $Ni(OH)_2$ oxidation wave (as is observed in the unpurified KOH), a decrease in the original anodic peak intensity and emergence of a new oxidation wave at more anodic potentials ($\sim$0.47 V vs Hg/HgO) is observed in the purified KOH (Figure 3d). No significant OER current is observed until >400 mV overpotential. Furthermore, Ni-$(OH)_2/NiOOH$ aged in the purified KOH shows a decrease in OER activity with increased aging time, opposite to what others have observed. The decrease in OER activity with aging may be due to a decrease in the number of active sites if they are associated with defects (e.g., stacking faults)[24,29,67,68] or edges[44,69] in the more-ordered β-$Ni(OH)_2$ films or due to reduced OH^-/O_2 transport rates within the interlayer volume. No Fe is observed in the XPS analysis of $Ni(OH)_2$ aged in the purified electrolyte. These data show that significant redox wave shifting and increases in OER activity only occur in the presence of Fe impurities and are not the result of formation of β-$Ni(OH)_2$. These results are important in the context of the theoretical effort that has been extended toward understanding the activity, electronic, and structural properties of Ni-based catalysts,[45,46,48,70−73] including experimental studies that have aimed to relate OER activity to fundamental properties such as the "oxophilicity" of the cation.[44]

The lack of OER activity until very positive potentials for the Fe-free NiOOH films reveals additional electrochemical features in the voltammetry. For the unaged film, a small oxidation peak at $\sim$0.6 V vs Hg/HgO is observed. Another small oxidation peak appears at $\sim$0.7 V vs Hg/HgO upon aging in concert with a larger peak at $\sim$0.47 V vs Hg/HgO. The wave at 0.6 V vs Hg/HgO may be due to the formation of a small amount of Ni^{4+}, perhaps at the edges of the α-$Ni(OH)_2/\gamma$-NiOOH sheets (or other sites representing only a small fraction of the Ni atoms). Revised Pourbaix diagrams for Ni suggest the formation of NiO_2 at OER potentials ($\eta > \sim$0.22 V) at pH 14,[74] and other studies have indicated the presence of Ni^{4+} at elevated potentials.[33−35,40,41,51,75] The oxidation waves that grow in at 0.47 and 0.7 V vs Hg/HgO are attributed to ordered β-NiOOH, as they arise in concert with the increased diffraction intensity due to β-$Ni(OH)_2$. The new oxidation waves were also observed in a film aged for 24 h (see Figure S9), which is the same film for which the GIXRD pattern is shown in Figure 2b. The small peak at 0.7 V vs Hg/HgO has not been reported previously, likely due to interference from the OER onset current when Fe impurities are present.

Previously, Corrigan also removed most Fe impurities from the electrolyte by prolonged electrolysis (5 days in a polypropylene container using a 1 kg Hg cathode 50 cm^2 and a 3 cm^2 high purity Ni anode, <0.005% Fe w/w).[18] The CV behavior he reported for $Ni(OH)_2/NiOOH$ films cycled in that purified electrolyte is similar to what we measure for films aged in our purified electrolyte, including the appearance of the peaks at 0.47 and 0.6 V vs Hg/HgO after aging. The new peak observed here at 0.7 V vs Hg/HgO appears to have been obscured by OER current in CVs collected by Corrigan,

6749

dx.doi.org/10.1021/ja502379c | *J. Am. Chem. Soc.* 2014, 136, 6744−6753

suggesting that the electrolyte purification used here is more effective at removing Fe.

In light of these findings, it is likely that previous studies of highly active $Ni(OH)_2$/NiOOH-based catalysts were affected by Fe impurities. For example, recent work has found that the Ni-borate (NiB_i) OER catalyst operating at pH 9.2 has a short-range structure analogous to that of NiOOH.[41,42,76] NiB_i requires prolonged anodization to reach its most active state. Using a combination of electrochemical and structural studies, it was argued that a significant population of Ni^{4+} is required for high OER activity and that the more-active anodized structure resembles that of γ-NiOOH rather than β-NiOOH.[41] These conclusions, like ours, are in conflict with the long-held view that β-NiOOH has a higher intrinsic OER activity. However, we conducted prolonged constant-current-density anodization of NiOOH in Fe-free KOH and found a decrease in activity over ~12 h at both 1 and 10 mA cm^{-2} (Figure S10). It is possible that the anodization of NiB_i films resulted in the incorporation of Fe from the electrolyte and that the increased activity of the anodized NiB_i catalyst is due to the formation of a mixed Ni–Fe oxyhydroxide. Further experiments on NiB_i under Fe-free conditions would be required to test this hypothesis.

3.3. Electronic Conductivity in $Ni_{1-x}Fe_xOOH$.

Electrocatalysts must be sufficiently conductive to pass charge through the catalyst film with a negligible potential drop. In cases where the catalyst is not sufficiently conductive, a portion of the applied potential will drop across the catalyst film to drive the current transport. This would lead to a lower apparent catalytic activity relative to a more-conductive film. It is known that NiOOH is conductive while $Ni(OH)_2$ is an insulator.[77] Corrigan hypothesized that Fe increases the conductivity of NiOOH, which might explain the enhanced activity of $Ni_{1-x}Fe_xOOH$ relative to NiOOH.[18] However, the conductivity of $Ni_{1-x}Fe_xOOH$ as a function of potential and Fe content has not previously been measured.

To measure the through-film conductivity *in situ* under relevant conditions, the films were deposited onto IDA electrodes. The two IDA leads were shorted together, and a total Au/Ti surface area of ~0.1 cm^2 was submerged in the deposition solution. Films were deposited at −0.1 mA cm^{-2} (cathodic) for 20 min. Deposition occurred on top of the IDA fingers and spanned the gap spaces (Figures 4a and 4b). After drying, cracking is observed due to contraction of the porous films. Dry films on the IDA electrodes were ~0.8−1.5 µm thick as determined by SEM and stylus profilometry. CVs were collected in a three-electrode configuration with the two IDA working electrodes shorted together (Figure 4c).

Steady-state *in situ* film conductivity measurements were performed by applying a constant potential offset between the two IDE working electrodes (WE1 and WE2) of 10 mV while WE1 was held constant relative to the reference electrode for 2−5 min until the measured current stabilized. During this dual-working-electrode conductivity experiment, the current measured at each working electrode can be described as the sum of faradaic and through-film-conduction components:

$$I_{WE1} = I_{OER1} + I_{cat1} + I_{cond} \qquad (1)$$

$$I_{WE2} = I_{OER2} + I_{cat2} - I_{cond} \qquad (2)$$

where I_{WE1} and I_{WE2} are the total currents measured at each working electrode, I_{OER} is the current from the OER, I_{cat} is the current from catalyst oxidation, and I_{cond} is the through-film

conductivity current. Because the working electrodes are symmetric, $I_{OER1} \approx I_{OER2}$ and $I_{cat1} \approx I_{cat2}$. Thus, $I_{WE1} - I_{WE2} \approx 2I_{cond}$. The effective catalyst film conductivities σ are estimated by

$$\sigma = \frac{I_{cond}w}{Nld\Delta V} \qquad (3)$$

where w is the IDA gap spacing, N is the number of electrodes (here $N = 130$), l is the length of each electrode, d is the film thickness, and ΔV is the voltage offset between WE1 and WE2 (here $\Delta V = 10$ mV).[78] We use the term effective conductivity to account for the fact that this calculation assumes a dense, uniform slab across the electrode array with a thickness much less than the spacing between the IDA electrode fingers such that current flows essentially linearly across the finger gap. Because these conditions are not rigorously met here, the values reported are taken as lower-bound estimates of the intrinsic conductivities.

The effective conductivities are shown in Figure 4d (conductivity data are shown with the y-axis on a logarithmic scale in Figure S11). All reduced films have low conductivities, independent of Fe concentration. A sharp increase in conductivity is observed upon Ni oxidation. The conductivity turn-on shifts to higher potentials with increasing Fe-content and correlates with the position of the $Ni^{2+/3+}$ oxidation wave (dashed lines, Figure 4d). Oxidized NiOOH under Fe-free conditions has $\sigma \approx 0.1$ to 0.2 mS cm^{-1}. Samples with 5%−25% Fe have $\sigma \approx 3.5$ to 6.5 mS cm^{-1}, all more than an order of magnitude higher than that of the Fe-free films. NiOOH films without intentionally added Fe measured in the unpurified electrolyte have $\sigma \approx 2.5$ mS cm^{-1}, consistent with substantial Fe incorporation over the duration of the dual-electrode *in situ* conductivity experiment.

These experiments show that Fe increases the conductivity of NiOOH. β-NiOOH is an n-type semiconductor,[79] and doping with Fe could change the carrier concentration (which may be consistent with the formation of a significant population of Fe^{4+} at anodic potentials; see discussion below). The 30−60-fold increase in conductivity would be expected to have a dramatic effect on the performance of NiOOH catalysts under conditions where the potential drop needed to transport current across the film was a substantial fraction of the total applied overpotential, i.e. for sufficiently thick films. For a 100 nm thick Fe-free NiOOH film passing a current density of 10 mA cm^{-2}, less than 1 mV would drop due to resistive losses. For typical films ~40 nm thick on Au substrates, we measure a ~200 mV difference between the overpotential required to drive 10 mA cm^{-2} for NiOOH versus $Ni_{0.75}Fe_{0.25}OOH$. The conductivity difference between NiOOH and $Ni_{0.75}Fe_{0.25}OOH$ cannot account for the difference in apparent activity. The conductivity differences would, however, be important for device architectures where much thicker films (i.e., ≫ 1 µm) are needed, and these measurements provide guidance for the design of such architectures.

3.4. Activity Enhancement via Partial-Charge Transfer between Ni and Fe.

Yeo and Bell compared the OER activity of NiOOH films with varying thicknesses and showed that on noble metal substrates the OER TOF increases for films with less than a few monolayers in thickness.[43] The effect was most pronounced on Au and smaller on less-electronegative Pd substrates. The increase in activity is attributed to partial electron transfer from the NiOOH to the more-electronegative noble metal substrate, thus modifying the electronic properties

of the Ni^{3+} centers. The effect is strongest for the first few monolayers because the cations are close to the substrate interface. Past a critical film thickness, the average Ni center was too far away from the interface to feel the electron-withdrawing effect of the substrate, and the measured activity was that of bulk NiOOH. Similarly, Gorlin et al. recently demonstrated enhanced activity of MnO$_x$ OER catalysts when combined with Au nanoparticles or by adding Au salt to the electrolyte.[80] The authors determined using electrochemical and X-ray absorption techniques that the observed activity enhancement is due to local electronic effects at the Au/MnO$_x$ interface.

Electrodeposited Ni–Fe mixed hydroxides contain Fe predominantly as Fe^{3+}.[33,36,81] Under OER conditions, E–pH (Pourbaix) diagrams predict both Fe^{3+} and Fe^{4+}.[82] In principle partial-charge transfer between Fe and Ni$^{3+/4+}$, as has been proposed by Corrigan et al.,[36] could enhance the activity via a similar mechanism as the Au support. In support of this hypothesis, the potential of the Ni$^{2+/3+}$ couple in Ni$_{1-x}$Fe$_x$OOH depends on the Fe content (e.g., see Figure 4c and also ref 8). Adding Fe makes it more difficult to oxidize Ni^{2+} leading to Ni$^{3+/4+}$ with more oxidizing power and thus possibly faster OER kinetics. If the Fe exerts a similar electron-withdrawing effect on Ni as does the Au substrate, the thickness-dependence of the OER TOF for NiOOH on Au observed by Yeo and Bell would be diminished after Fe incorporation because the Fe would be distributed throughout the film (thus "activating" all Ni centers).

Figure 5 compares the TOF as a function of thickness for Fe-free NiOOH and Ni$_{0.75}$Fe$_{0.25}$OOH on Au and GC. The number
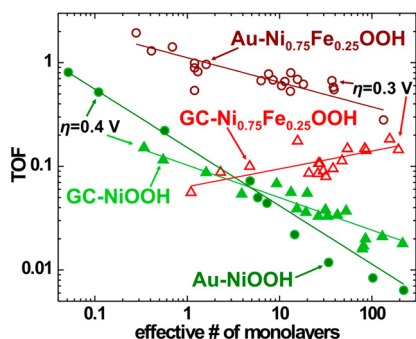

Figure 5. Turnover frequency (TOF) as a function of film thickness for Fe-free NiOOH (closed symbols) and Ni$_{0.75}$Fe$_{0.25}$OOH (open symbols). Films on Au (circles) show a greater thickness dependence than films on GC (triangles) for both catalysts. Lines are fit to the data using a power function $y = ax^b$ (see Supporting Information for fit values). TOF values were calculated at $\eta = 0.3$ V for Ni$_{0.75}$Fe$_{0.25}$OOH and $\eta = 0.4$ V for NiOOH.

of active sites was assumed to be equal to the number of electrochemically active Ni sites obtained from integration of the Ni$^{2+/3+}$ wave. The slopes of the fit lines indicate the magnitude of the TOF thickness dependence. For both catalysts, the thickness dependence is greater on Au than on GC, consistent with the higher work function of Au compared to C (Au 5.1–5.5 eV; C 5.0 eV).[83] The difference in work function for the electrode surface in a base under oxidizing conditions, however, is likely different from those of the pure elements measured in vacuum due to surface oxidation of the Au to form AuO$_x$ (which is seen in CV scans; see Figure S3) and the possibility of oxidation of the C and contamination by

adventitious adsorbed hydrocarbon species. Another explanation for the activity enhancement is the formation of a bimetallic Au–Ni oxide/hydroxide at the electrode surface, which Yeo and Bell consider based on in situ Raman measurements.[43] The lower activity on the GC substrates could be due to the inability of C and Ni to form such a bimetallic oxide under these conditions.

Figure 5 also shows that for both substrates the TOF thickness dependence is less for Ni$_{0.75}$Fe$_{0.25}$OOH than for the NiOOH. On Au, the TOF increases by more than 2 orders of magnitude for NiOOH over the measured thickness range, while the TOF for Ni$_{0.75}$Fe$_{0.25}$OOH changes by less than an order of magnitude. On C, the NiOOH TOF increases by about an order of magnitude over the thickness range measured, while Ni$_{0.75}$Fe$_{0.25}$OOH shows no significant change with film thickness. These results are consistent with the hypothesis that the Fe enhances the activity of NiOOH through a Ni–Fe partial-charge-transfer activation process occurring throughout the film similar to that which occurs for thin layers on Au.

Corrigan et al. found evidence from in situ Mössbauer spectroscopy of partial electron transfer away from Fe^{3+} accompanying the oxidation of Ni^{3+} to Ni^{4+}.[36] There is substantial evidence from X-ray absorption[33,41,75] and Mössbauer[34–36] experiments that Ni^{4+} and/or Fe^{4+} are present in Ni$_{1-x}$Fe$_x$OOH at OER potentials. Axmann and Glemser studied Ni$_{1-x}$Fe$_x$OOH using Mössbauer spectroscopy and found high-spin Fe^{4+} without observing quadrupole splitting, indicating a regular (i.e., no Jahn–Teller distortion) octahedral geometry around Fe.[34] The authors propose a model to explain their results whereby clusters of one regular Fe^{IV}O$_6$ octahedron surrounded by six regular Ni^{IV}O$_6$ octahedra create discrete M^{4+} domains within sheets that otherwise consist of M^{3+} ions. It may be that such M^{4+} domains within Ni$_{1-x}$Fe$_x$OOH are the OER active sites. Further experimental and theoretical study to measure the electronic density of states, map the domain structure, and identify reaction intermediates with changes in Fe content is needed to better describe the electronic structure of Ni$_{1-x}$Fe$_x$OOH.

4.0. CONCLUSIONS

We tested several mechanisms by which Fe has been predicted to increase the catalytic activity of Ni(OH)$_2$/NiOOH for the OER. We showed that the conductivity of Ni(OH)$_2$/NiOOH increases by >30-fold upon coprecipitation with Fe, but that these differences cannot explain the observed increase in activity. The effect of film thickness on TOF was investigated, and it was found that films with codeposited Fe showed a lower thickness-dependence on Au or GC substrates than Fe-free films. This is consistent with an Fe-induced partial-charge-transfer mechanism, which activates Ni centers throughout the catalyst film. We studied the structure and activity of Ni$_{1-x}$Fe$_x$(OH)$_2$/Ni$_{1-x}$Fe$_x$OOH films as a function of aging. All films studied showed an increase in crystallinity with aging, while only those exposed to Fe impurities showed an increase in OER activity. This shows that the absorption of Fe impurities is responsible for the dramatic increase in activity of aged Ni(OH)$_2$/NiOOH and disproves the long-held view that β-NiOOH is intrinsically more active for the OER than γ-NiOOH. The results also indicate that previous reports of highly active Ni(OH)$_2$-based OER catalysts include Fe impurities. Long range order (or disorder), however, is apparently unimportant to the catalytic activity in the

$Ni_{1-x}Fe_xOOH$ system. These results further underscore the importance of recognizing and accounting for the effects of impurities on the performance of heterogeneous electrocatalysts. They are also important for comparison with theoretical predictions and ultimately a complete understanding of the origins of high activity in $Ni_{1-x}Fe_xOOH$-based OER electrocatalysts.

ASSOCIATED CONTENT

Supporting Information

Figures S1−S11 and fit equations for the data in Figure 5 are included in the Supporting Information. This material is available free of charge via the Internet at http://pubs.acs.org.

AUTHOR INFORMATION

Corresponding Author

swb@uoregon.edu

Notes

The authors declare no competing financial interest.

ACKNOWLEDGMENTS

REFERENCES

(1) Walter, M. G.; Warren, E. L.; McKone, J. R.; Boettcher, S. W.; Mi, Q.; Santori, E. A.; Lewis, N. S. *Chem. Rev.* **2010**, *110*, 6446.

(2) Cook, T. R.; Dogutan, D. K.; Reece, S. Y.; Surendranath, Y.; Teets, T. S.; Nocera, D. G. *Chem. Rev.* **2010**, *110*, 6474.

(3) Suntivich, J.; May, K. J.; Gasteiger, H. A.; Goodenough, J. B.; Shao-Horn, Y. *Science* **2011**, *334*, 1383.

(4) McCrory, C. C. L.; Jung, S. H.; Peters, J. C.; Jaramillo, T. F. *J. Am. Chem. Soc.* **2013**, *135*, 16977.

(5) Landon, J.; Demeter, E.; Inoglu, N.; Keturakis, C.; Wachs, I. E.; Vasic, R.; Frenkel, A. I.; Kitchin, J. R. *ACS Catal.* **2012**, *2*, 1793.

(6) Kim, T. W.; Choi, K.-S. *Science* **2014**, *343*, 990.

(7) Gong, M.; Li, Y.; Wang, H.; Liang, Y.; Wu, J. Z.; Zhou, J.; Wang, J.; Regier, T.; Wei, F.; Dai, H. *J. Am. Chem. Soc.* **2013**, *135*, 8452.

(8) Louie, M. W.; Bell, A. T. *J. Am. Chem. Soc.* **2013**, *135*, 12329.

(9) Smith, R. D. L.; Prévot, M. S.; Fagan, R. D.; Trudel, S.; Berlinguette, C. P. *J. Am. Chem. Soc.* **2013**, *135*, 11580.

(10) Smith, R. D. L.; Prévot, M. S.; Fagan, R. D.; Zhang, Z.; Sedach, P. A.; Siu, M. K. J.; Trudel, S.; Berlinguette, C. P. *Science* **2013**, *340*, 60.

(11) Trotochaud, L.; Ranney, J. K.; Williams, K. N.; Boettcher, S. W. *J. Am. Chem. Soc.* **2012**, *134*, 17253.

(12) Merrill, M. D.; Dougherty, R. C. *J. Phys. Chem. C* **2008**, *112*, 3655.

(13) Kleiman-Shwarsctein, A.; Hu, Y. S.; Stucky, G. D.; McFarland, E. W. *Electrochem. Commun.* **2009**, *11*, 1150.

(14) Corrigan, D. A. *Hydrogen Generator Having a Low Oxygen Overpotential Electrode.* U.S. Patent 4,882,024, Nov. 21, 1989.

(15) Trotochaud, L.; Mills, T. J.; Boettcher, S. W. *J. Phys. Chem. Lett.* **2013**, *4*, 931.

(16) Lin, F.; Boettcher, S. W. *Nat. Mater.* **2014**, *13*, 81.

(17) Mills, T. J.; Lin, F.; Boettcher, S. W. *Phys. Rev. Lett.* **2014**, *112*, 148304.

(18) Corrigan, D. A. *J. Electrochem. Soc.* **1987**, *134*, 377.

(19) Corrigan, D. A.; Bendert, R. M. *J. Electrochem. Soc.* **1989**, *136*, 723.

(20) Haber, J. A.; Cai, Y.; Jung, S.; Xiang, C.; Mitrovic, S.; Jin, J.; Bell, A. T.; Gregoire, J. M. *Energy Environ. Sci.* **2014**, *7*, 682.

(21) Santos, D. M. F.; Amaral, L.; Šljukić, B.; Macciò, D.; Saccone, A.; Sequeira, C. A. C. *J. Electrochem. Soc.* **2014**, *161*, F386.

(22) Xiang, C.; Suram, S. K.; Haber, J. A.; Guevarra, D. W.; Soedarmadji, E.; Jin, J.; Gregoire, J. M. *ACS Comb. Sci.* **2014**, *16*, 47.

(23) Gerken, J. B.; Chen, J. Y. C.; Massé, R. C.; Powell, A. B.; Stahl, S. S. *Angew. Chem., Int. Ed.* **2012**, *51*, 6676.

(24) Tessier, C.; Haumesser, P. H.; Bernard, P.; Delmas, C. *J. Electrochem. Soc.* **1999**, *146*, 2059.

(25) McEwen, R. S. *J. Phys. Chem.* **1971**, *75*, 1782.

(26) Notten, P. H. L. In *Interstitial Intermetallic Alloys*; Grandjean, F., Long, G., Buschow, K. H. J., Eds.; Springer: Netherlands, 1995; Vol. *281*, p 151.

(27) Bernard, M. C.; Bernard, P.; Keddam, M.; Senyarich, S.; Takenouti, H. *Electrochim. Acta* **1996**, *41*, 91.

(28) de Moura, A. P.; Lima, R. C.; Paris, E. C.; Li, M. S.; Varela, J. A.; Longo, E. *J. Solid State Chem.* **2011**, *184*, 2818.

(29) Delmas, C.; Tessier, C. *J. Mater. Chem.* **1997**, *7*, 1439.

(30) Gourrier, L.; Deabate, S.; Michel, T.; Paillet, M.; Hermet, P.; Bantignies, J. L.; Henn, F. *J. Phys. Chem. C* **2011**, *115*, 15067.

(31) Hall, D. S.; Lockwood, D. J.; Poirier, S.; Bock, C.; MacDougall, B. R. *J. Phys. Chem. A* **2012**, *116*, 6771.

(32) Kim, M. S.; Kim, K. B. *J. Electrochem. Soc.* **1998**, *145*, 507.

(33) Balasubramanian, M.; Melendres, C. A.; Mini, S. *J. Phys. Chem. B* **2000**, *104*, 4300.

(34) Axmann, P.; Glemser, O. *J. Alloys Compd.* **1997**, *246*, 232.

(35) Demourgues-Guerlou, L.; Fournès, L.; Delmas, C. *J. Solid State Chem.* **1995**, *114*, 6.

(36) Corrigan, D. A.; Conell, R. S.; Fierro, C. A.; Scherson, D. A. *J. Phys. Chem.* **1987**, *91*, 5009.

(37) Subbaraman, R.; Danilovic, N.; Lopes, P. P.; Tripkovic, D.; Strmcnik, D.; Stamenkovic, V. R.; Markovic, N. M. *J. Phys. Chem. C* **2012**, *116*, 22231.

(38) Kenney, M. J.; Gong, M.; Li, Y. G.; Wu, J. Z.; Feng, J.; Lanza, M.; Dai, H. J. *Science* **2013**, *342*, 836.

(39) Yeo, B. S.; Bell, A. T. *J. Phys. Chem. C* **2012**, *116*, 8394.

(40) Lu, P. W. T.; Srinivasan, S. *J. Electrochem. Soc.* **1978**, *125*, 1416.

(41) Bediako, D. K.; Lassalle-Kaiser, B.; Surendranath, Y.; Yano, J.; Yachandra, V. K.; Nocera, D. G. *J. Am. Chem. Soc.* **2012**, *134*, 6801.

(42) Bediako, D. K.; Surendranath, Y.; Nocera, D. G. *J. Am. Chem. Soc.* **2013**, *135*, 3662.

(43) Yeo, B. S.; Bell, A. T. *J. Am. Chem. Soc.* **2011**, *133*, 5587.

(44) Subbaraman, R.; Tripkovic, D.; Chang, K.-C.; Strmcnik, D.; Paulikas, A. P.; Hirunsit, P.; Chan, M.; Greeley, J.; Stamenkovic, V.; Markovic, N. M. *Nat. Mater.* **2012**, *11*, 550.

(45) Busch, M.; Ahlberg, E.; Panas, I. *Catal. Today* **2013**, *202*, 114.

(46) Busch, M.; Ahlberg, E.; Panas, I. *Phys. Chem. Chem. Phys.* **2011**, *13*, 15062.

(47) Bajdich, M.; García-Mota, M.; Vojvodic, A.; Nørskov, J. K.; Bell, A. T. *J. Am. Chem. Soc.* **2013**, *135*, 13521.

(48) Li, Y.-F.; Selloni, A. *ACS Catal.* **2014**, *4*, 1148.

(49) Sauerbrey, G. *Z. Phys. A: Hadrons Nucl.* **1959**, *155*, 206.

(50) Wehrens-Dijksma, M.; Notten, P. H. L. *Electrochim. Acta* **2006**, *51*, 3609.

(51) Corrigan, D. A.; Knight, S. L. *J. Electrochem. Soc.* **1989**, *136*, 613.

(52) Lyons, M. E. G.; Brandon, M. P. *Int. J. Electrochem. Sci.* **2008**, *3*, 1386.

(53) Kostecki, R.; McLarnon, F. *J. Electrochem. Soc.* **1997**, *144*, 485.

(54) Rajamathi, M.; Kamath, P. V.; Seshadri, R. *J. Mater. Chem.* **2000**, *10*, 503.

(55) Desilvestro, J.; Corrigan, D. A.; Weaver, M. J. *J. Electrochem. Soc.* **1988**, *135*, 885.

6752

dx.doi.org/10.1021/ja502379c | *J. Am. Chem. Soc.* 2014, 136, 6744−6753

(56) Godwin, I. J.; Lyons, M. E. G. *Electrochem. Commun.* **2013**, *32*, 39.

(57) Trotochaud, L.; Boettcher, S. W. *Scr. Mater.* **2014**, *74*, 25.

(58) Nakahira, A.; Kubo, T.; Murase, H. *IEEE Trans. Magn.* **2007**, *43*, 2442.

(59) Li, Y.; Li, H.; Yang, M.; He, X.; Ni, P.; Kang, L.; Liu, Z.-H. *Appl. Clay Sci.* **2011**, *52*, 51.

(60) Iwasaki, T.; Yoshii, H.; Nakamura, H.; Watano, S. *Appl. Clay Sci.* **2012**, *58*, 120.

(61) Trolard, F.; Bourrié, G. In *Clay Minerals in Nature - Their Characterization, Modification and Application*; Valaskova, M., Ed.; InTech: 2012; pp 171−188.

(62) Nan, J.; Yang, Y.; Lin, Z. *Electrochim. Acta* **2006**, *51*, 4873.

(63) Doyle, R. L.; Godwin, I. J.; Brandon, M. P.; Lyons, M. E. G. *Phys. Chem. Chem. Phys.* **2013**, *15*, 13737.

(64) McBreen, J.; O'Grady, W. E.; Tourillon, G.; Dartyge, E.; Fontaine, A.; Pandya, K. I. *J. Phys. Chem.* **1989**, *93*, 6308.

(65) Nazri, G.; Corrigan, D. A.; Maheswari, S. P. *Langmuir* **1989**, *5*, 17.

(66) Lo, Y. L.; Hwang, B. J. *Langmuir* **1998**, *14*, 944.

(67) Casas-Cabanas, M.; Rodriguez-Carvajal, J.; Canales-Vazquez, J.; Palacin, M. R. *J. Mater. Chem.* **2006**, *16*, 2925.

(68) Deabate, S.; Henn, F.; Devautour, S.; Giuntini, J. C. *J. Electrochem. Soc.* **2003**, *150*, J23.

(69) Subbaraman, R.; Tripkovic, D.; Strmcnik, D.; Chang, K. C.; Uchimura, M.; Paulikas, A. P.; Stamenkovic, V.; Markovic, N. M. *Science* **2011**, *334*, 1256.

(70) Van der Ven, A.; Morgan, D.; Meng, Y. S.; Ceder, G. *J. Electrochem. Soc.* **2006**, *153*, A210.

(71) Hermet, P.; Gourrier, L.; Bantignies, J. L.; Ravot, D.; Michel, T.; Deabate, S.; Boulet, P.; Henn, F. *Phys. Rev. B* **2011**, *84*, 235211.

(72) Man, I. C.; Su, H.-Y.; Calle-Vallejo, F.; Hansen, H. A.; Martínez, J. I.; Inoglu, N. G.; Kitchin, J.; Jaramillo, T. F.; Nørskov, J. K.; Rossmeisl, J. *ChemCatChem* **2011**, *3*, 1159.

(73) Greeley, J.; Nørskov, J. K. *J. Phys. Chem. C* **2009**, *113*, 4932.

(74) Beverskog, B.; Puigdomenech, I. *Corros. Sci.* **1997**, *39*, 969.

(75) Capehart, T. W.; Corrigan, D. A.; Conell, R. S.; Pandya, K. I.; Hoffman, R. W. *Appl. Phys. Lett.* **1991**, *58*, 865.

(76) Risch, M.; Grimaud, A.; May, K. J.; Stoerzinger, K. A.; Chen, T. J.; Mansour, A. N.; Shao-Horn, Y. *J. Phys. Chem. C* **2013**, *117*, 8628.

(77) Natan, M. J.; Belanger, D.; Carpenter, M. K.; Wrighton, M. S. *J. Phys. Chem.* **1987**, *91*, 1834.

(78) Nishizawa, M.; Ise, T.; Koshika, H.; Itoh, T.; Uchida, I. *Chem. Mater.* **2000**, *12*, 1367.

(79) Madou, M. J.; Mckubre, M. C. H. *J. Electrochem. Soc.* **1983**, *130*, 1056.

(80) Gorlin, Y.; Chung, C.-J.; Benck, J. D.; Nordlund, D.; Seitz, L.; Weng, T.-C.; Sokaras, D.; Clemens, B. M.; Jaramillo, T. F. *J. Am. Chem. Soc.* **2014**, *136*, 4920.

(81) Kim, S.; Tryk, D. A.; Antonio, M. R.; Carr, R.; Scherson, D. *J. Phys. Chem.* **1994**, *98*, 10269.

(82) Schweitzer, G. K.; Pesterfield, L. L. *The Aqueous Chemistry of The Elements*; Oxford University Press: Oxford, 2010.

(83) *CRC Handbook of Chemistry and Physics*, 76th ed.; Lide, D. R., Ed.; CRC Press: Boca Raton, FL, 1995.